Investigation of constitutive relationship and dynamic recrystallization behavior of 22MnB5 during hot deformation

Yakun Xu[a], Peter Birnbaum[b], Stefan Pilz[c], Xincun Zhuang[a,d], Zhen Zhao[a,d,*], Verena Kräusel[b,*]

[a] Institute of Forming Technology and Equipment, School of Materials Science and Engineering, Shanghai Jiao Tong University, Shanghai 200030, China
[b] Institute for Machine Tools and Production Processes (IWP), Chemnitz University of Technology, Chemnitz 09107, Germany
[c] Institute for Complex Materials (ICM), Leibniz-Institute for Solid State and Materials Research Dresden (IFW Dresden), Dresden 01069, Germany
[d] National Engineering Research Center of Die & Mold CAD, Shanghai Jiao Tong University, Shanghai 200030, China

ARTICLE INFO

ABSTRACT

In order to analyze the softening behavior of 22MnB5 steel and further predict the constitutive relationship during hot sheet metal forming, a series of isothermal hot compression tests were conducted at the temperature range of 800–950 °C and strain rate range of 0.01–0.8 s^{-1} on BAEHR 805 A/D thermo-mechanical simulator system. Based on the friction corrected flow curves, the characteristic strain and stress of dynamic recrystallization (DRX) were derived from the Kocks-Mecking plots and expressed as a function of Zener-Hollomon parameter. Moreover, a physical constitutive model considering work hardening (WH), dynamic recovery (DRV) and DRX as well as corresponding JMAK-type DRX kinetics were developed. The results showed that the established physical equations can accurately predict the flow behavior with a correlation coefficient of 0.997 and average absolute relative error of 3.89%. Optical observation of the microstructure after hot compression revealed that the established DRX kinetics accurately reflects the reality, and then a Zener-Hollomon parameter dependent dynamic recrystallized grain size model was developed. Furthermore, EBSD analysis was carried out to study the effect of deformation conditions on martensite morphology and the results show that a lower temperature and higher strain rate lead to a finer martensite packet while the martensite block width becomes larger under the higher strain rate.

Introduction

Due to the increasing demands for vehicle lightweight, better safety and crash performance, the need for a good performance structural of components which, are formed from ultra-high strength steels (UHSS) and advanced high strength steels (AHSS) associated with complex forming processes, is apparent. Difficulties such as low formability, high forming load and large spring back during cold forming of the UHSS and AHSS, force the manufacturers to look for new solutions [1]. The combination of hot sheet metal forming and innovative press technology provide new opportunities for the production of high-strength structural parts with complex shapes [2]. Accordingly, a novel hot sheet metal forming technology combined press hardening process with cushion-ram pulsation (CRP) was proposed as a promising solution to these problems, allowing higher forming limitation and lower loads [3–5]. Here a superposition takes place of rapid in-die quenching and simultaneous deep drawing with low-frequency oscillatory motion

(< 2 Hz). Wrinkling in the component can be avoided, and significantly greater drawing depths are achieved compared to conventional hot forming [4]. Thanks to the stepwise forming pattern, austenitized blanks experience the recovery and softening during the short stops of drawing tools and the phenomenon of work hardening (WH), dynamic recovery (DRV) and dynamic recrystallization (DRX) of the materials occur during the whole process [5]. Moreover, it is known that microstructure evolution of austenite strongly affects the phase transformation kinetics and the final mechanical properties of the products [6]. To better understanding these complex thermo-mechanical behaviors and optimize the novel hot sheet metal forming process, it is necessary to study the constitutive models considered softening mechanisms and the microstructure evolution of the AHSS during the hot forming.

22MnB5 steel as the most common used advanced high strength steel for the press hardening process, numerous researches on the establishment of precise constitutive models are reported. Åkerström et al. developed a Nemat-Nasser model for boron steels by hot

compression tests and an inverse modeling [7]. Naderi et al. conducted isothermal uniaxial compression test on a Baehr DIL system and established two constitutive models known as the Voce-Kocks and the Molinari-Ravichandran models to describe the plastic behavior of 22MnB5 [8]. Nguyen et al. proposed a modification of Johnson-Cook model by combining the Ludwick and Voce's hardening law and used a VUMAT subroutine to verify the accuracy of the developed model [9]. Li et al. performed isothermal uniaxial tension of the boron steel B1500HS at the temperature range of 20–900 °C and a modified Arrhenius model as well as the Johnson-Cook model were developed to describe the flow behavior of B1500HS with different microstructure composition [10]. Zhou et al. evaluated two constitutive models on the basis of the results from isothermal uniaxial tensile tests performed on 22MnB5, namely, a strain-compensated Arrhenius-type constitutive model and a set of unified viscoplastic model, and concluded that the best fit of the experimental data is attained with the strain-compensated Arrhenius-type constitutive model [11]. Zhang et al. determined a modified Fiel-Backofen's constitutive model for 22MnB5 steel which considered the effect of strain, strain rate and volume fraction of quenched microconstituents [12]. However, most of the previous models only focused on the hardening behavior of the boron steels, while the softening effect caused by the DRV and DRX are neglected.

In this study, 22MnB5 steel was investigated by isothermal compression tests at varied temperatures and strain rate. A physical constitutive model and corresponding JMAK-type DRX kinetics were established based on the friction corrected flow curves and their prediction accuracy was verified by comparing with experimental data. Moreover, the dependences of the characteristic stress and strain values of DRX on temperature and strain rate were discussed. The DRXed grain size was modelling by measn of Avrime model. Finally, the effect of hot deformation conditions on the martensite morphology formed after hot compression and quenching were analyzed by austenite reconstruction algorithm with EBSD analysis.

Experimental procedure

The chemical composition (wt%) of commercial 22MnB5 investigated in this study is summarized in Table 1. The initial microstructure of 22MnB5 steel in the normalized state, which consisted of equiaxial ferrite and globulitic pearlite, is shown in Fig. 1. Compression specimens with 10 mm in length and 5 mm in diameter were machined with the longitudinal axis in rolling direction. To study the DRX behavior of 22MnB5 steel, the machined cylinder samples were compressed with a BAEHR 805 A/D thermal-mechanical simulator (as shown in Fig. 2(a)) according to the temperature schedule represented in Fig. 2(b). Considering the main forming window of the austenited workpieces during the press hardening with CRP technology, temperature range of 800–950 °C was taken. The specimens were initially heated under vacuum with a rate of 3 K/s up to 950 °C followed by 300 s soaking time for full austenization. Then the specimens were cooled to the deformation temperature at the cooling rate of 25 K/s and kept at that temperature for 10 s to eliminate the temperature gradient. The tests were performed to a true strain of 1 at 800 °C, 850 °C, 900 °C, and 950 °C with a strain rate of 0.01 s^{-1}, 0.1 s^{-1}, and 0.8 s^{-1}, respectively. Additionally, CCT diagram of 22MnB5 calculated by JMatPro was illustrated in Fig. 2(b) for comparison with the temperature history

Table 1
Chemical composition of studied 22MnB5.

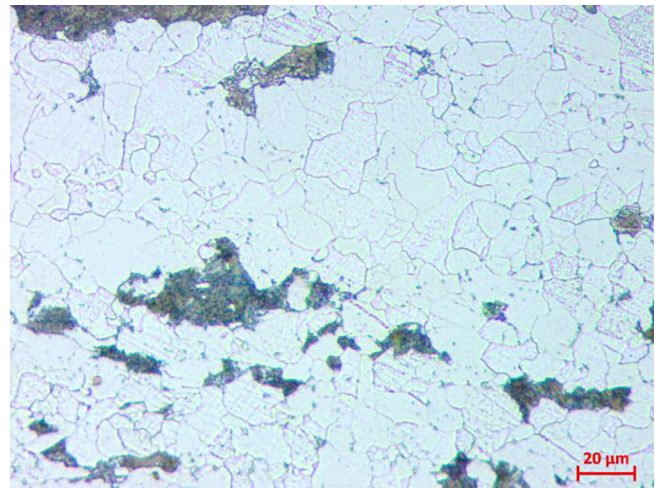| C	Si	Mn	P	S	Al	Ti	Nb
0.2028	0.3712	1.162	0.0135	0.00196	0.05718	0.0325	0.00308
B	Cr	Cu	Mo	Ni	Ta	W	V
0.00146	0.2688	0.0301	0.03936	0.05882	0.00736	0.005	0.0045

Fig. 1. Microstructure of the as-received 22MnB5 steel (parallel to deformation direction).

of the cooling process to guarantee the full martensite transformation after hot compression test. Afterwards, compressed samples were quenched by high pressure argon and sliced along the axial section. All sliced specimens were etched with picric acid solution (280 ml deionized water, 5.5 g picric acid, 8.4 ml Teepol and 2 ml hydrochloric acid) to reveal prior austenite grain boundaries. Optical microstructure was observed by using Zeiss Axio Vert.A1 MAT. And the grain size was determined by line intercept method according to ASTM E112. Finally, EBSD studies were conducted using a Zeiss Gemini 1530 FEG-SEM equipped with an EBSD detector (Bruker e-Flash^{HR}) to investigate martensite microstructure. For the analysis of the EBSD data sets, the free texture and crystallography analysis toolbox MTEX (v 5.1.1) were used [13]. Grain maps were calculated with a 3° minimum grain boundary threshold. Parent austenite grain boundaries (PAGB) as well as packet and block boundaries of martensite were calculated with the parent austenite grain (PAG) reconstruction algorithm developed by Nyyssönen et al. [14].

Results and discussion

Flow behavior

It is well know that the interfacial friction between the sample and anvils is unavoidable during the compression process. With the increase of deformation degree, the dimension of contact surface between specimen and anvils increases, which results in severe heterogeneous deformation i.e. barreling and bulging [15,16]. Therefore, the measured flow curves are corrected by considering the effects of interfacial friction. Fig. 3 shows the geometries of the specimens before and after hot deformation process, the initial height and radius of samples are named as h_O and R_O, respectively. After hot deformation test, the height of samples is compressed to h. While R_{fri} and R_{max} are the radius of surface and the maximum section of deformed samples. In this case, the measured flow stress can be corrected by following equation [17]:

$$\sigma = \frac{\sigma_m C^2}{2[\exp(C) - C - 1]} \tag{1}$$

where σ and σ_m are the corrected and measured flow stresses, respectively. C is the correction coefficient considering interfacial friction. $C = 2mR/h$. R is the ideal radius of deformed sample without friction, $R = R_0\sqrt{h_0/h}$. And the friction coefficient m can be described by following equations [18]:

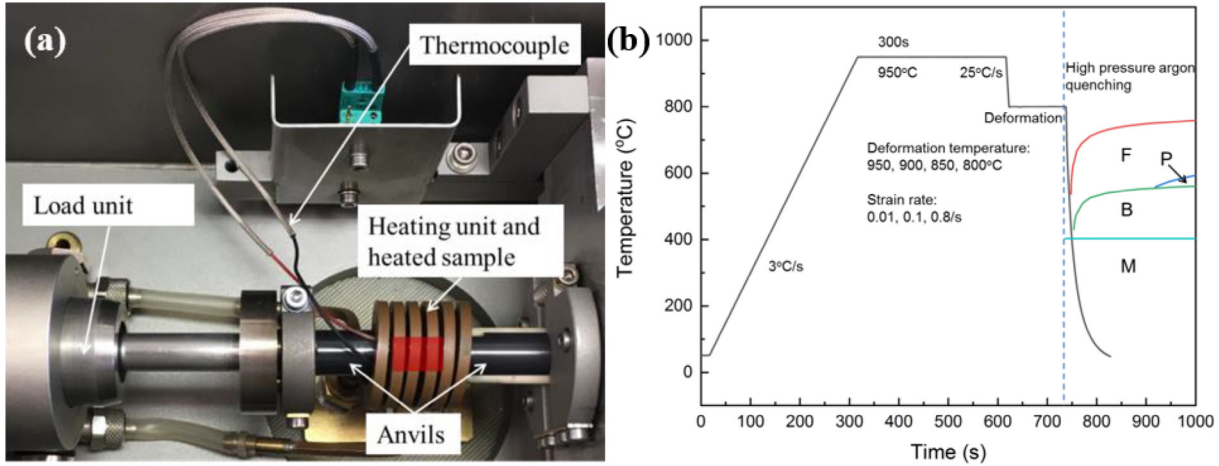$$m = \frac{(R/h)b}{(4/\sqrt{3}) - (2b/3\sqrt{3})} \tag{2}$$

Fig. 2. (a) Experiment set up and (b) schematic diagram of hot compression process and CCT diagram of 22MnB5 steel.
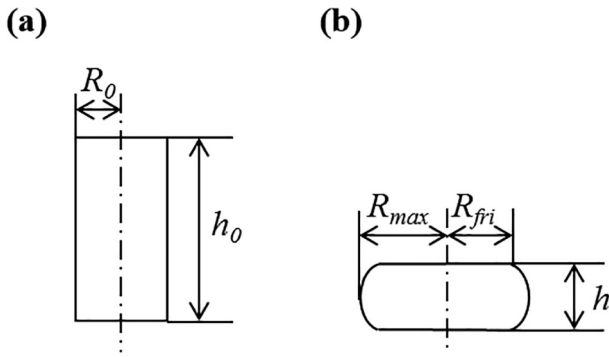

Fig. 3. Geometries of specimens: (a) before hot compression; (b) after hot compression.

where

$$b = 4\frac{\Delta R}{R} \cdot \frac{h}{\Delta h} \qquad (3)$$

and $\Delta R = R_{max} - R_{fri}$, $\Delta h = h_0 - h$. Due to the side folding over of the deformed samples, the value of R_{fri} is difficult to measure in practice [15]. Therefore, top radius R_{fri} can be determined empirically by following equation:

$$R_{fri} = \sqrt{3\frac{h_0}{h}R_0^2 - 2R_{max}^2} \qquad (4)$$

Other parameters including R_0, R_{max}, h_0 and h can be measured directly from the deformed samples. Based on above method, an average value $m = 0.42$ was calculated. Then the flow stress under different deformation conditions can be modified by considering the effects of the interface friction between specimens and anvils. Corrected flow curves were fitted with a 7th order polynomial beginning from the yield strain (ε_0) which was identified from the experimental engineering strain stress in terms of a 0.2% plastic strain (as it shows in Fig. 4(a)). Fig. 4(b)–(d) show the corrected flow curves of 22MnB5 steel under different strain rates and different deformation temperatures. Obviously, the stress is significantly sensitive to the temperature and strain rate, and all the flow curves exhibit a typical DRX behavior. In the initial deformation stage, the flow stress increases rapidly due to the continuous increasing amount and accumulation of dislocation. With further deformation, the stress increasing rate decreases for the appearance of DRV and DRX until reaching peak stress (σ_p). The effect of dislocation annihilation increases but is still weaker than that of dislocation multiplication before reaching peak stress. When the softening rate exceeds the hardening rate, the flow stress gradually decreases to a

steady state (σ_s), which means the work hardening and dynamic softening reach a dynamic balance. Furthermore, it is clear that the flow stress declines with the increase of deformation temperature or the decrease of strain rate. The reason behind this can be attributed to following two aspects. On the one hand, elevated temperature significantly promotes the mobility of the metal atoms and grain boundary, and thus the DRX process is accelerated. Meanwhile, the DRX induced by the slip and climb of dislocation is enhanced by thermal activation. Hence, the flow stress decreases with the increase of forming temperature. On the other hand, reduction of deformation time caused by high strain rate hinders the growth of DRX grains and increases the work hardening effect, which finally leads to an increase of flow stress [19].

Characteristic strain and stress

Determination of characteristic points and Zener-Hollomon parameter

As mentioned above, there are several characteristic points including the yield stress (σ_0), critical strain (ε_c) and stress (σ_c) of DRX, peak strain (ε_p) and stress (σ_p), steady stress (σ_{ss}) and saturation stress (σ_{sat}) of DRV, which are of important for the qualification of DRV and DRX. To determine those characteristic values, the work hardening rate ($\theta = d\sigma/d\varepsilon$) was calculated from the corrected flow curves and plots of strain hardening rate with respect to stress (Kocks-Mecking plots) was employed. Based on the methods proposed by Poliak and Jonas [20], the critical stress for the initiation of DRX was identified as the inflection point of the $\theta - \sigma$ curve which can be obtained from the zero point of second derivative of Kocks-Mecking plots. Similarly, the peak stress and steady stress can be attained from $\theta - \sigma$ curve when the work hardening rate reaches zero (as it shown in Fig. 5(a)) [21–23]. Additionally, the dash line, which is extrapolated from the linear part before σ_c, is assumed to be the work hardening rate when only work hardening and dynamic recovery occur. In this case, the saturated stress (σ_{sat}) of DRV is achieved when the dash line reaches zero. The correlation between θ and σ for the different deformation conditions is shown in Fig. 5.

Generally, the combined effect of the temperature and strain rate on the hot deformation behavior of metals and alloys can be characterized by the Zener-Hollomon parameter. The expression of Zener-Hollomon parameter (Z) is given as:

$$Z = \dot{\varepsilon}\exp(Q_{act}/RT) \qquad (5)$$

where $\dot{\varepsilon}$ is the strain rate (s^{-1}), Q_{act} is the activation energy (J·mol^{-1}), R is the universal gas constant (8.314 J·mol^{-1}K^{-1}) and T is the absolute temperature (K). Additionally, the relationship between true stress, strain rate and deformation temperature can be described by the well-
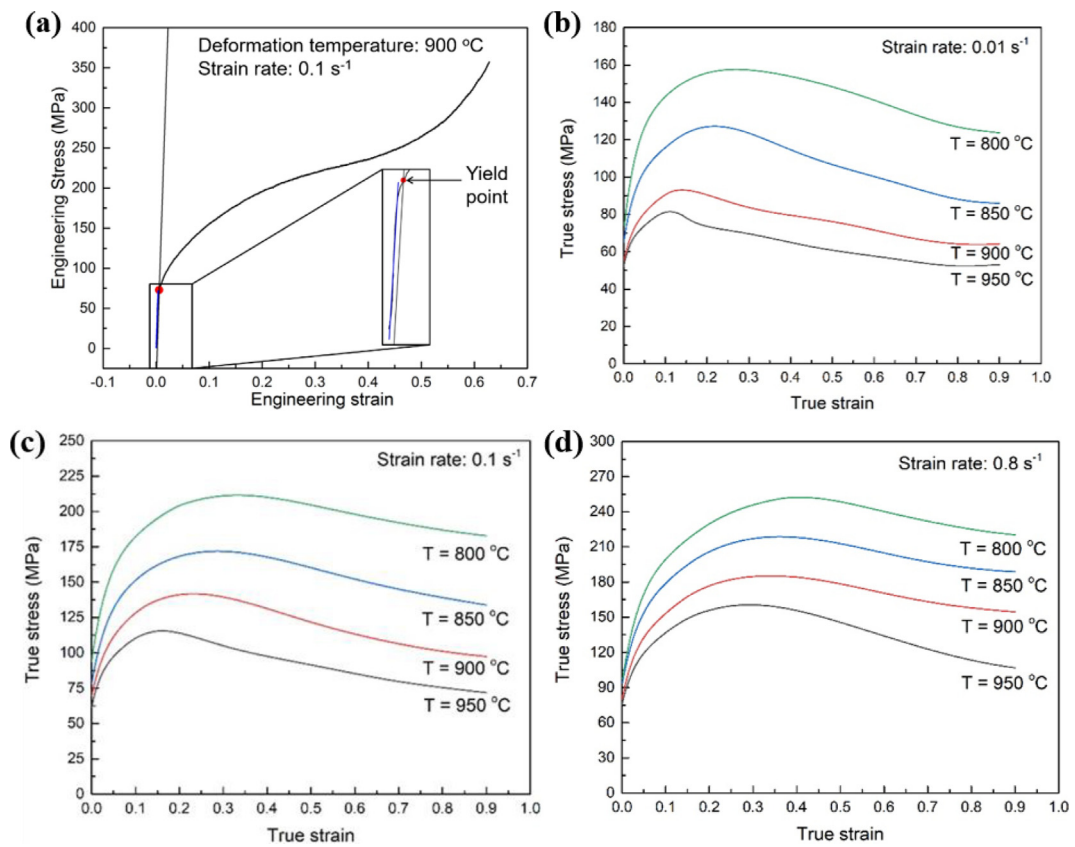
Fig. 4. Determination of yield point (a) and true stress-strain curves of 22MnB5 steel under different deformation temperatures at the same strain rates (b) 0.01 s^{-1} (c) 0.1 s^{-1} (d) 0.8 s^{-1}.
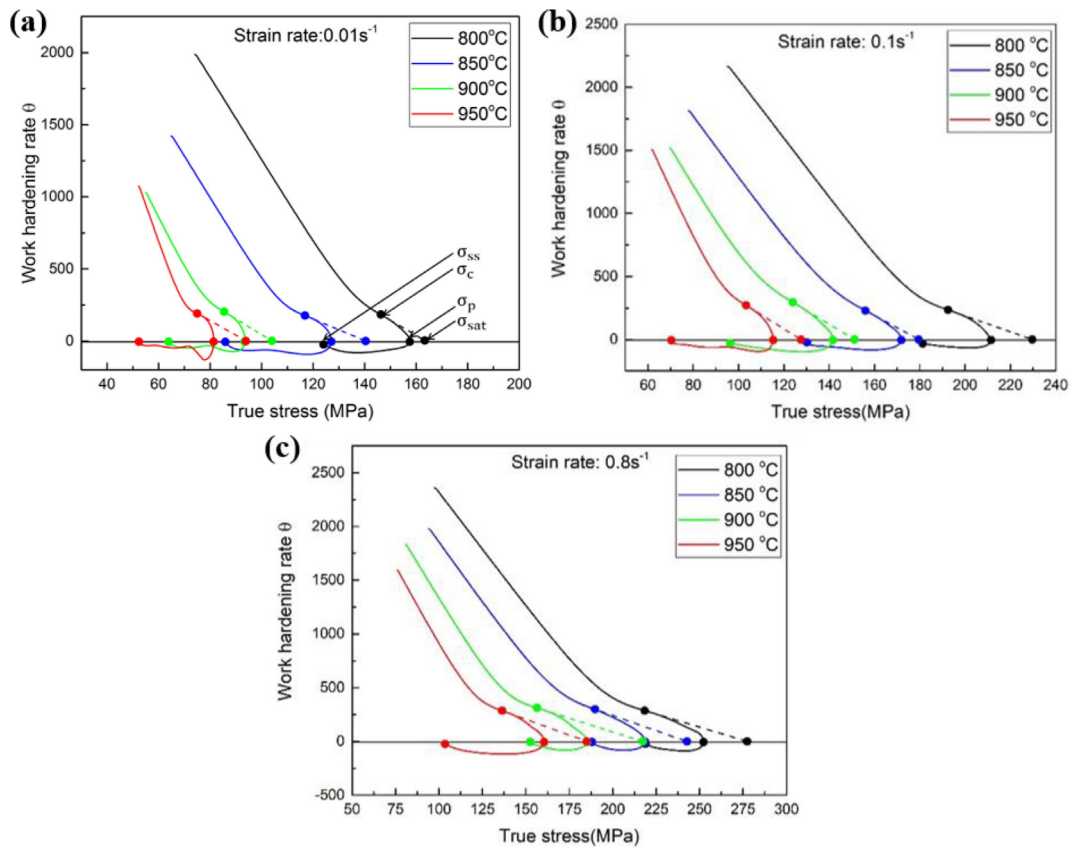

Fig. 5. Work hardening rate versus true stress under different deformation temperatures at the same strain rate (a) 0.01 s^{-1} (b) 0.1 s^{-1} (c) 0.8 s^{-1}.

known Arrhenius equations [24]:

$$\dot{\varepsilon} = AF(\sigma)\exp(-Q_{act}/RT) \tag{6}$$

$$F(\sigma) = \begin{cases} \sigma^{n_1} & \alpha\sigma < 0.8 \\ \exp(\beta\sigma) & \alpha\sigma > 1.2 \\ [\sinh(\alpha\sigma)]^{n_2} & \text{for all } \sigma \end{cases} \tag{7}$$

σ is the flow stress, α, β, A and n are the material parameters and α can be evaluated by $\alpha = \beta/n_1$. Generally, the maximum stress σ_p is used for the determination of those material parameters. Taking natural logarithm of the equations and after building the partial derivative, these material parameters can be expressed by:

$$n_1 = \left. \frac{\partial\ln\dot{\varepsilon}}{\partial\ln\sigma_p} \right|_{T=constant} \tag{8}$$

$$\beta = \left. \frac{\partial\ln\dot{\varepsilon}}{\partial\sigma_p} \right|_{T=constant} \tag{9}$$

$$n_2 = \left. \frac{\partial\ln\dot{\varepsilon}}{\partial\ln[\sinh(\alpha\sigma_p)]} \right|_{T=constant} \tag{10}$$

$$Q_{act} = Rn_2 \left. \frac{\partial\ln[\sinh(\alpha\sigma_p)]}{\partial(1/T)} \right|_{\dot{\varepsilon}=constant} \tag{11}$$

As illustrated in Fig. 6, the values for $n_1 = 7.551$, $\beta = 0.04937$ ($\alpha = \beta/n_1 = 0.00654$) and $n_2 = 5.617$ are obtained from the average slope of $\ln\dot{\varepsilon}$ versus $\ln\sigma_p$, $\ln\dot{\varepsilon}$ versus σ_p and $\ln\dot{\varepsilon}$ versus $\ln[\sinh(\alpha\sigma_p)]$, respectively. According to the Eq. (11), the activation energy Q_{act} of 22MnB5 steel was obtained with a value of $316.331 \text{kJ}\cdot\text{mol}^{-1}$.

Characteristic strains and stress

Based on the methods described above, the values for ε_c and ε_p under different deformation conditions are obtained (listed in Table 2).

Table 2
The values of ε_c and ε_p under different deformation conditions.

$\dot{\varepsilon}/s^{-1}$	$T/°C$	ε_c	ε_p
0.01	800	0.11629	0.26954
	850	0.10673	0.217
	900	0.07081	0.14253
	950	0.05553	0.11078
0.1	800	0.13891	0.30436
	850	0.11944	0.28695
	900	0.08454	0.23184
	950	0.06953	0.16293
0.8	800	0.15689	0.4097
	850	0.13341	0.36165
	900	0.11061	0.32439
	950	0.09896	0.29219

It is found that ε_c and ε_p increase with the decrease of temperature or the increase of strain rate, which also can be described as a higher Z value. Hence, it indicates that the characteristic strain can be represented as a function of Zener-Hollomon parameter [21,25,26]. Fig. 7(a) illustrates regression plots and the dependence of ε_c and ε_p on Z can be attained:

$$\varepsilon_c = 0.002752 \cdot Z^{0.1167} \tag{12}$$

$$\varepsilon_p = 0.002377 \cdot Z^{0.150} \tag{13}$$

Additionally, Jorge Jr. and Balancin suggested that the mechanical parameters of the hot forming can be described by a simple equation with Zener-Hollomon parameter [27].

$$\text{Parameter} = C \cdot Z^m \tag{14}$$

Accordingly, the dependences of all characteristic stresses on Z are shown in Fig. 7. And following equations can be developed by
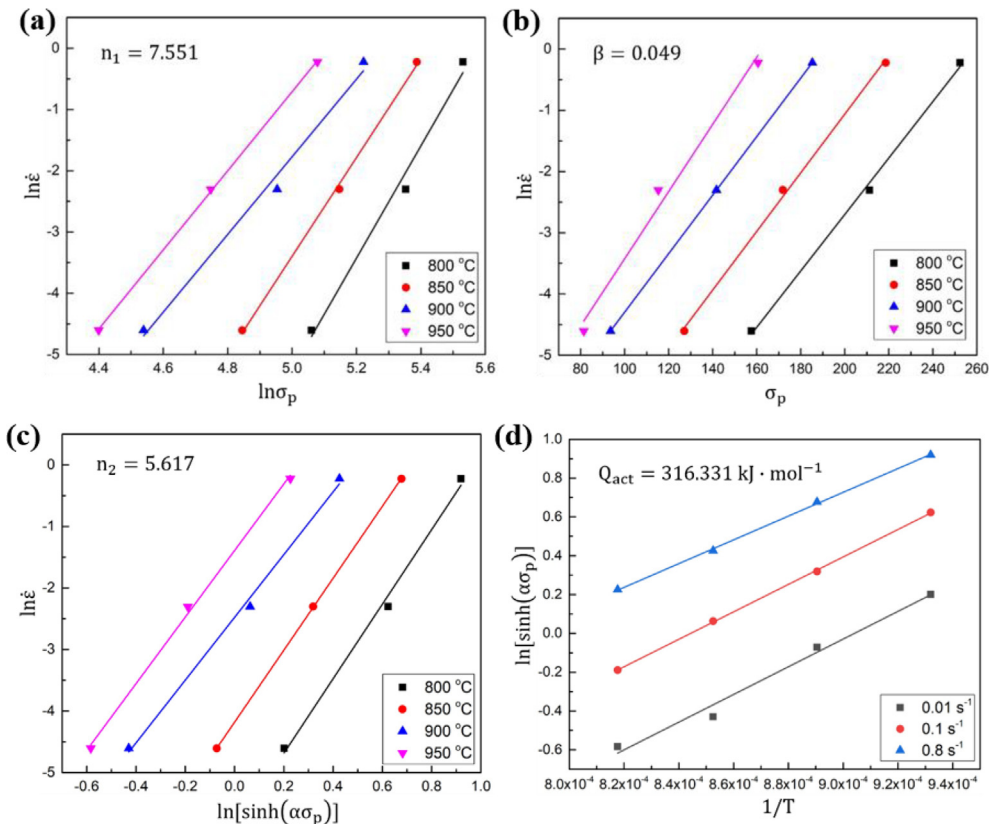

Fig. 6. Linear fitted plots for determination of (a) n_1, (b) β, (c) n_2 and (d) Q_{act}.
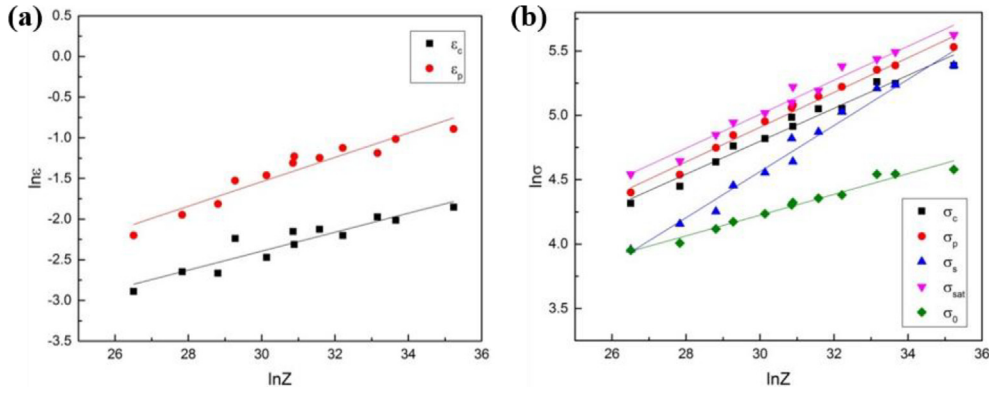
Fig. 7. Dependence of characteristic parameters and Z.

regression analysis:

$$\sigma_0 = 6.10257 \cdot Z^{0.08054} \tag{15}$$

$$\sigma_c = 2.60278 \cdot Z^{0.12807} \tag{16}$$

$$\sigma_p = 2.3690 \cdot Z^{0.13485} \tag{17}$$

$$\sigma_{ss} = 0.44398 \cdot Z^{0.17916} \tag{18}$$

$$\sigma_{sat} = 2.84226 \cdot Z^{0.13213} \tag{19}$$

The relationships between the characteristic stress and Zener-Hollomon parameter can be simply described using power-law equations. In addition, it is obvious that a higher Z value, i.e. lower deformation temperature or higher strain rate, leads to an increase of the characteristic strain and stress.

Constitutive modeling of flow curve

It has been pointed out that the DRX occurs when the accumulated dislocation density exceeds a critical value, namely the critical strain. However, before the critical strain, the evolution of the dislocation density (ρ) in metal or alloys during hot deformation is a competition result between the generation of WH and the annihilation of DRV. Bergström and Aronsson developed a model to evaluate the evolution of the dislocation density in WH-DRV stage which is given as [28]:

$$\frac{d\rho}{d\varepsilon} = h - r\rho \tag{20}$$

where h is the thermal work-hardening rate representing the storage of dislocation caused by WH, and it can be regarded as a material constant with respect to the strain, r represents the rate of DRV. Additionally, the dependence of flow stress on ρ is expressed by $\sigma = \alpha\mu b \sqrt{\rho}$ [29,30]. By integrating the above equation based on the methods from Alberto et al. and Lin et al., the flow stress during WH and DRV period can be attained as [27,31,32]:

$$\sigma_{WH\text{-}DRV} = [\sigma_{sat}^2 - (\sigma_{sat}^2 - \sigma_0^2)\exp(-r\varepsilon)]^{0.5} \ (\varepsilon < \varepsilon_c) \tag{21}$$

This model characterize the constitutive relationship during hot deformation when DRX has not occurred yet. According to Eq. (21), the value of r can be determined by the following derived equation:

$$r\varepsilon = \ln\left(\frac{\sigma_{sat}^2 - \sigma_0^2}{\sigma_{sat}^2 - \sigma^2}\right)(\varepsilon < \varepsilon_c) \tag{22}$$

Since σ_{sat} and σ_0 has been obtained above, by importing the strain as well as corresponding stress before critical strain and afterwards performing linear regression, the value of r under different hot forming conditions was calculated. The dependence of r on Z is illustrated in Fig. 8. It is indicated that r can be represented as a function of Z, i.e.
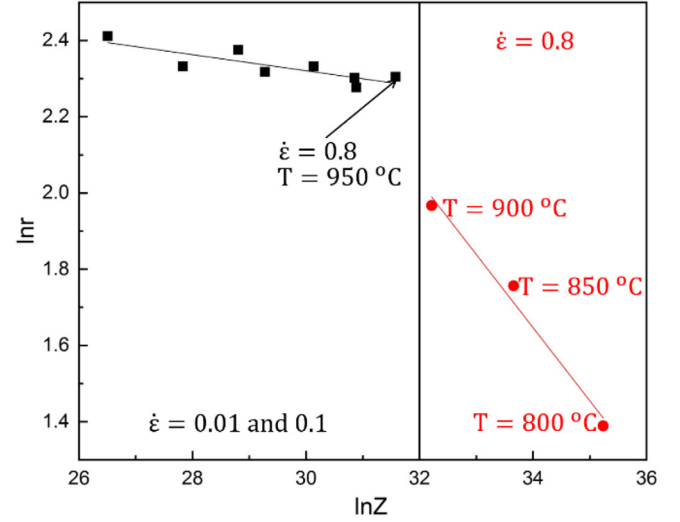
Fig. 8. Correlation between DRV rate r on Z.

$$r = \begin{cases} 19.716 \cdot Z^{-0.02109} & Z < 7.89E13 \\ 3544.527 \cdot Z^{-0.19195} & Z > 7.89E13 \end{cases} \tag{23}$$

It is of interest that the DRV coefficient is a piecewise function of Z and with the increase of Z, the recovery rate r decreases generally but with different slope in different range of Z. When lnZ is less than 32, which indicates the lower strain rate (0.01 s^{-1} and 0.1 s^{-1}), r decreases slightly with the increase of Z, while r decreases sharply with the increasing Z when lnZ is greater than 32. It is known that the extent of recovery is governed by deformation conditions and material characteristics such as stacking fault energy (SFE). The vacancies and dislocation mobility depends on the SFE, which, by affecting the extent of dislocation dissociates, determines the rate of dislocation climb and cross slip [33]. At elevated temperature, which also named low Z value, the value of SFE increases, climb is rapid and significant DRV may occur, leading to a high value of r. Additionally, different sensitivity of r on the strain rate is also attributed to the extent of dislocation climb and cross slip. High strain rates indicate a short time for atom migration which inhibits the annihilation of defects, resulting in a faster decline of r. However, when the temperature reaches 950 °C at strain rate of 0.8 s^{-1}, the effect of thermal energy dominates which shows a higher DRV rate and a lower slope compared with that under 800 °C–900 °C at strain rate of 0.8 s^{-1}.

Once the amount of accumulated dislocations exceeds the critical value, dynamic recrystallized nucleation and grain growth will take place near the grain boundaries, twin boundaries, as well as the deformation bands. Generally, the relationship between volume fraction of dynamic recrystallization and strain can be expressed by well-known

Johnson-Mehl-Avrami-Kolmogorov (JMAK) equation [34,35]:

$$X_{drx} = 1 - \exp\left[-\beta_d\left(\frac{\varepsilon - \varepsilon_c}{\varepsilon_{0.5}}\right)^{k_d}\right] (\varepsilon \geq \varepsilon_c)$$
(24)

where X_{drx} is the volume fraction of DRX grains, ε is the true strain and $\varepsilon_{0.5}$ is the required strain for a volume fraction of 50% for DRX. β_d and k_d are the Avrami material parameters. Meanwhile, the volume fraction of DRX can be also estimated by the softening effect of flow stress [36].

$$X_{drx} = \frac{\sigma_{WH\cdot DRV} - \sigma}{\sigma_{sat} - \sigma_s} \quad (\varepsilon \geq \varepsilon_c)$$
(25)

$\sigma_{WH\cdot DRV}$ is flow stress when only work hardening and dynamic recovery occur. After combining Eqs. (24) and (25), the flow stress during DRX period can be obtained:

$$\sigma = \sigma_{WH} - (\sigma_{sat} - \sigma_s)\left\{1 - \exp\left[-\beta_d\left(\frac{\varepsilon - \varepsilon_c}{\varepsilon_{0.5}}\right)^{k_d}\right]\right\}(\varepsilon \geq \varepsilon_c)$$
(26)

By substituting r, σ_0, σ_{sat} and the strain that is larger than the critical value into Eq. (21) and combining Eq. (25), $\varepsilon_{0.5}$ and X_{drx} under the four different temperatures and three strain rates were calculated. Furthermore, the dependence of $\varepsilon_{0.5}$ on Z is shown in Fig. 9 and the following equation can be obtained simultaneously:

$$\varepsilon_{0.5} = \begin{cases} 0.003254 \cdot Z^{0.16601} & Z < 7.89E13 \\ 0.115178 \cdot Z^{0.0455} & Z > 7.89E13 \end{cases}$$
(27)

Owing to the separation expression of r, $\varepsilon_{0.5}$ is also characterized as a piecewise function of Z. Taking natural logarithm on Eq. (24), the DRX material parameters of β_d and k_d can be determined by the fitted line of $\ln[-\ln(1 - X_{drx})]$ versus $\ln[(\varepsilon - \varepsilon_c)/\varepsilon_{0.5}]$ as illustrated in Fig. 10. Finally, the values of β_d and k_d were calculated as 1.14951 and 1.90834, respectively. Therefore, the constitutive and DRX models for the 22MnB5 steel during the WH-DRV and DRX period can be summarized as follows:
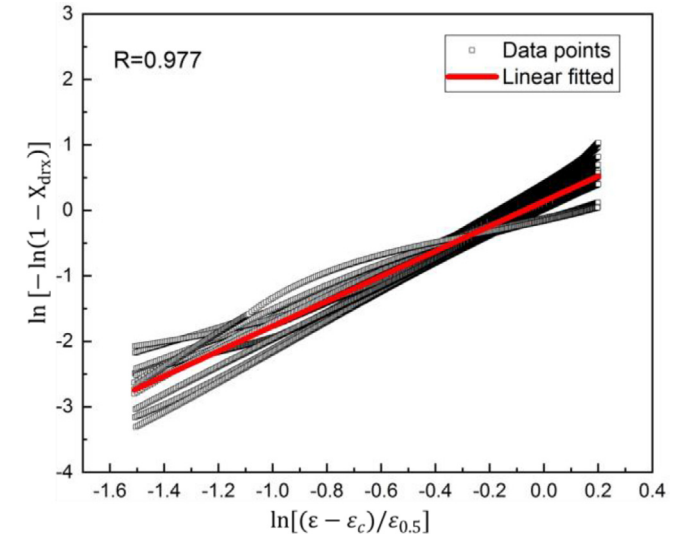

Fig. 10. Dependence between $\ln[-\ln(1 - X_{drx})]$ and $\ln[(\varepsilon - \varepsilon_c)/\varepsilon_{0.5}]$.

$$\begin{cases} \sigma_{WH\cdot DRV} = [\sigma_{sat}^2 - (\sigma_{sat}^2 - \sigma_0^2)\exp(-r\varepsilon)]^{0.5} \\ \sigma_{DRX} = \sigma_{WH\cdot DRV} - (\sigma_{sat} - \sigma_s)\left\{1 - \exp\left[-1.14951\left(\frac{\varepsilon - \varepsilon_c}{\varepsilon_{0.5}}\right)^{1.90834}\right]\right\} \\ X_{drx} = 1 - \exp\left[-1.14951\left(\frac{\varepsilon - \varepsilon_c}{\varepsilon_{0.5}}\right)^{1.90834}\right] \\ Z = \dot{\varepsilon}\exp(\frac{316331}{RT}) \\ \sigma_{sat} = 2.84226 \cdot Z^{0.13213} \\ \varepsilon_c = 0.002752 \cdot Z^{0.1167} \\ \sigma_0 = 6.10257 \cdot Z^{0.08054} \\ \sigma_s = 0.44398 \cdot Z^{0.17916} \\ \varepsilon_{0.5} = \begin{cases} 0.003254 \cdot Z^{0.16601} & Z < 7.89E13 \\ 0.115178 \cdot Z^{0.0455} & Z > 7.89E13 \end{cases} \\ r = \begin{cases} 19.716 \cdot Z^{-0.02109} & Z < 7.89E13 \\ 3544.527 \cdot Z^{-0.19195} & Z > 7.89E13 \end{cases} \end{cases}$$
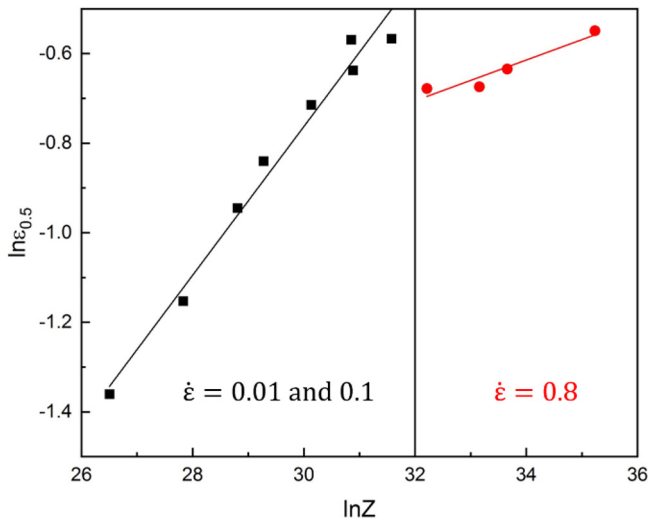(28)

Accordingly, the dependence of X_{drx} on strain under different deformation temperature and strain rate, considering the established model, is illustrated in Fig. 11. Obviously, the typical sigmodal curves of DRX can be observed. Regardless the deformation, the volume fraction of DRX increases to 100% gradually with the increasing strain in most tests. For a certain strain, a higher temperature or a lower strain rate is beneficial to obtain a higher value of X_{drx}, because of the increased grain boundary mobility and sufficient time for atomic diffusion. Consequently, a larger deformation degree is needed for a completed DRX when the deformation temperature is decreased or the strain rate is increased. Additionally, it is important to mention that almost all of the tests can achieve over 80% dynamic recrystallization fraction volume at the strain of 0.9, which is a little bit higher than that of common microalloyed steel [37]. This is on the one hand due to the addition of boron in 22MnB5 steel. According to Mejía and Jacuinde, DRX can be accelerated by the addition of boron which leads to the solid solution softening at high strains [38]. On the other hand, the retarding effect of fine carbide precipitation at the grain boundary mainly caused by Nb, Cr, Mo, and V elements is well known [39]. However, in the studied material the amount of these elements is negligible. Thus, dragging effect on the grain boundary caused by precipitationsis not significant.

In order to verify the accuracy of the developed constitutive model for 22MnB5 steel, the correlation coefficient (R) and the average
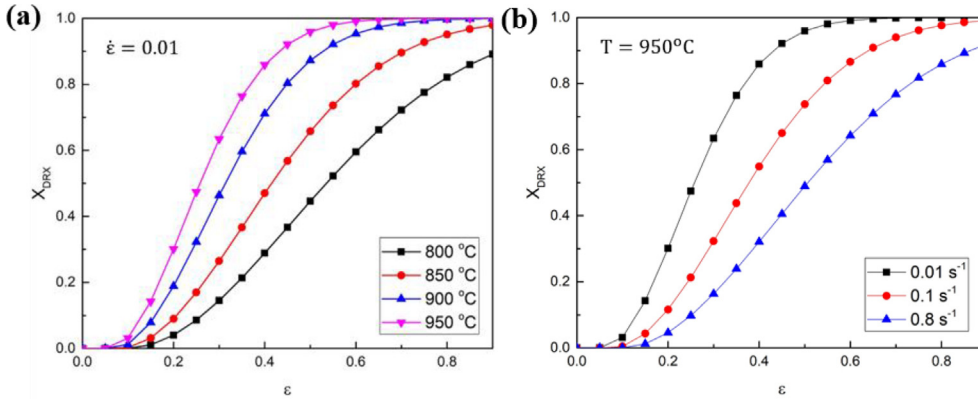

Fig. 9. Dependence between $\varepsilon_{0.5}$ and Z.

Fig. 11. The relationship between X_{drx} and ε at (a) different temperatures and (b) strain rates.
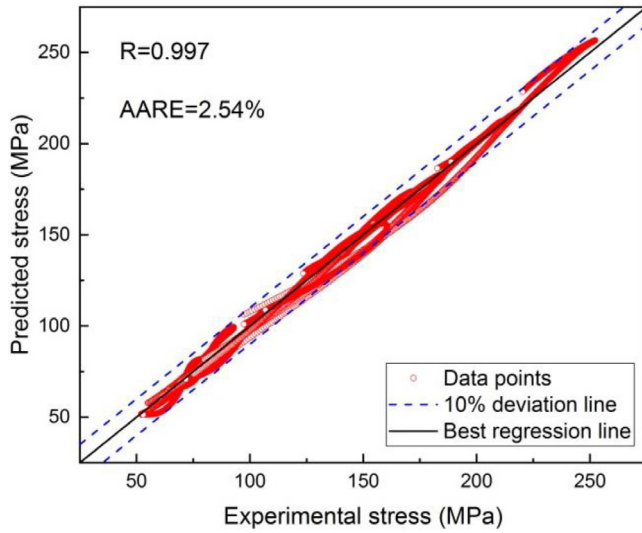

Fig. 12. The comparison between predicted stress and experimental stress.

absolute relative error (AARE) are calculated as 0.997 and 2.54% according to Eqs. (29) and (30), respectively. Where σ_{Ei} is experimental stress, σ_{Pi} is the predicted stress and N is the number of data points, $\bar{\sigma}_{Ei}$ and $\bar{\sigma}_{Pi}$ represent mean values of σ_{Ei} and σ_{Pi} [40]. Therefore, the comparison between predicted flow stresses obtained by the constitutive model and experimental flow stresses is implemented in Fig. 12. It is obvious that most of the predicted values lie close to the best regression line ($\sigma_{Pi} = \sigma_{Ei}$) and in the area within the 10% deviation lines, which indicates that the developed constitutive model can effectively predict the flow stress of 22MnB5 steel at elevated temperature.

$$R = \frac{\sum_{i=1}^{N} (\sigma_{Ei} - \bar{\sigma}_{Ei})(\sigma_{Pi} - \bar{\sigma}_{Pi})}{\sqrt{\sum_{i=1}^{N} (\sigma_{Ei} - \bar{\sigma}_{Ei})^2 \sum_{i=1}^{N} (\sigma_{Pi} - \bar{\sigma}_{Pi})^2}} \qquad (29)$$

$$AARE(\%) = \frac{1}{N} \sum_{i=1}^{N} \left| \frac{\sigma_{Pi} - \sigma_{Ei}}{\sigma_{Ei}} \right| \qquad (30)$$

Microstructure observation

The microstructure of the undeformed austenite and samples that underwent different hot compression tests are shown in Fig. 13, with the corresponding mean grain sizes and standard deviation listed in Table 3. As is shown in Fig. 13(a), fine equiaxed grains with an average grain size around 13.08 μm can be realized by austenization of the samples for 300 s at a temperature of 950 °C with a heating rate of 3 K/s. Moreover, the typical wavy or corrugated grain boundaries and small grains at triple points of prior grains are observed in Fig. 13(b)–(d)

which indicates the recrystallized grains after hot compression [41]. Considering Fig. 13(b)–(d), it is obvious that higher temperatures results in an increased grain size. The main reason is that the mobility of the grain boundaries is promoted with higher thermal energy, which makes the grain growth more easier. On the other hand, a higher strain rate during hot compression leads to fine grain generation. The reason is that a high strain rate enhances the work hardening rate, which increases the substructure caused by the accumulated dislocations and provides more nucleation sites for the new grains. Additionally, a higher strain rate means unsufficient incubation time for the dislocations proliferation, subgrains nucleation and rotation is drastically reduced with the rise strain rate [42]. Thus, more fine grains are formed in the matrix, just as shown in Fig. 13(d)–(f). While some tiny grains bulged between the grains, boundaries can be found (as shown in Fig. 13(d)), which indicates the nucleation and growth of recrystallized grains [43]. Based on the above analysis, it is concluded that the size of dynamic recrystallized grains (D_{DRXed}) strongly depends on the deformation temperature and strain rate. Similar to the mechanical parameters of hot deformation, D_{DRXed} should also have a close dependence on the Zener–Hollomon parameter. Consistent with expectations, the relationship between D_{DRXed} and Z parameter is shown in Fig. 14. Simultaneously, following equation is achieved based on the linear fitting of the measured grain size:

$$D_{DRXed} = 1288.50769 \cdot Z^{-0.16783} \qquad (31)$$

Effect of deformation condition on martensite morphology

During press hardening processes, die quenching is performed simultaneous to the deep drawing process. As a result of the high cooling rates and in combination with phase transformation, a complex martensitic microstructure is generated, afterwards. The microstructure which consists of lath martensite is divided into packets, blocks and laths. The parent austenite grains (PAG) are thereby subdivided by packets. Each packet consists of various laths, which share the same habit plane and is normally further subdivided in blocks. The laths in a block are separated by a low-angle boundary with a misorientation of few degrees. The packet size affects both the strength and toughness of low-carbon steels like 22MnB5 with a microstructure of lath martensite. The block size is considered as a key factor to determine the strength ascribed to the block boundary strengthening [44]. To study the influence of the deformation temperature and the strain rate on the martensite morphology, EBSD measurements were conducted for the samples with deformation at 850 °C/0.01 s^{-1}, 950 °C/0.01 s^{-1}, 950 °C/0.8 s^{-1} and an overall strain of $\varepsilon = 1$.

Representative subsets of the measured orientation mappings are shown in Fig. 15(a–c). For the parent austenite grain boundaries (PAGB), the packet boundaries and the block boundaries were calculated according to the algorithm developed by Nyyssönen et al. [14]. They are illustrated together with the corresponding band-contrast
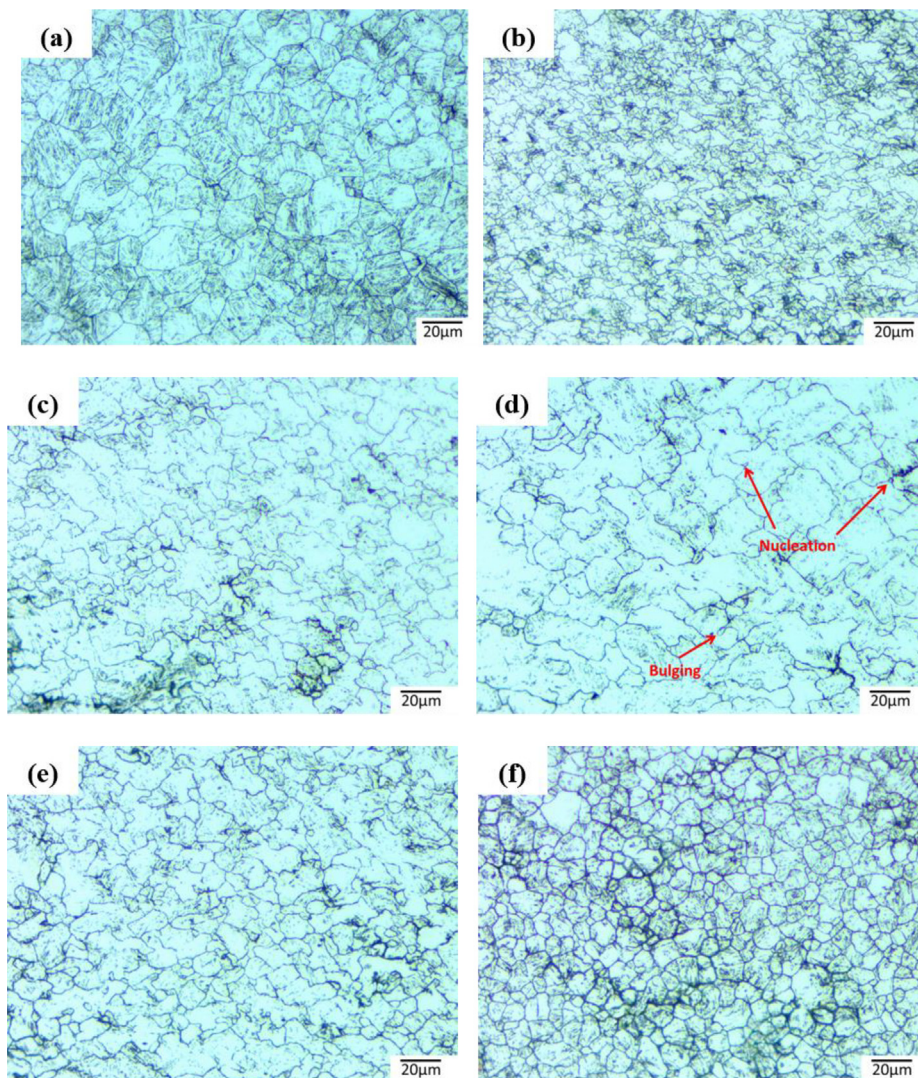
Fig. 13. Microstructure of 22MnB5 steel (a) before hot compression test, hot compressed at (b) 850 °C/0.01 s^{-1}, (c) 900 °C/0.01 s^{-1} (d) 950 °C/0.01 s^{-1} (e) 950 °C/0.1 s^{-1} (f) 950 °C/0.8 s^{-1}.

Table 3
Mean grain size and standard deviation of initial and compressed austenite of 22MnB5 steel.

Figure	(a)	(b)	(c)	(d)	(e)	(f)
Temperature/°C	950	850	900	950	950	950
Strain rate/S^{-1}	–	0.01	0.01	0.01	0.1	0.8
Grain size/μm	13.08	8.51	11.92	15.83	10.22	7.77
STD/μm	1.39	0.62	1.33	0.85	1.87	0.15

mapping in Fig. 15(d–f). As it shown in Fig. 15, the "sub-grain like" martensite microstructure complicates a quantitative analysis of the recrystallized volume fraction. Further criteria to determine the DRX volume like the grain orientation spread (GOS) or the grain average misorientation (GAM) are not recommended either. However, qualitative conclusions for the DRX and the martensitic substructure can be derived from the EBSD measurements.

The orientation mapping of the sample deformed at 850 °C with a strain rate of 0.01 s^{-1} (Fig. 15(a)) reveals that in some grains (marked with white arrows) clear orientation gradients are still present after the hot deformation and the subsequent martensitic transformation. In addition, subgrain boundaries with a wavy or globulitic morphology, which is uncommon for lath martensite, can be observed in the band-
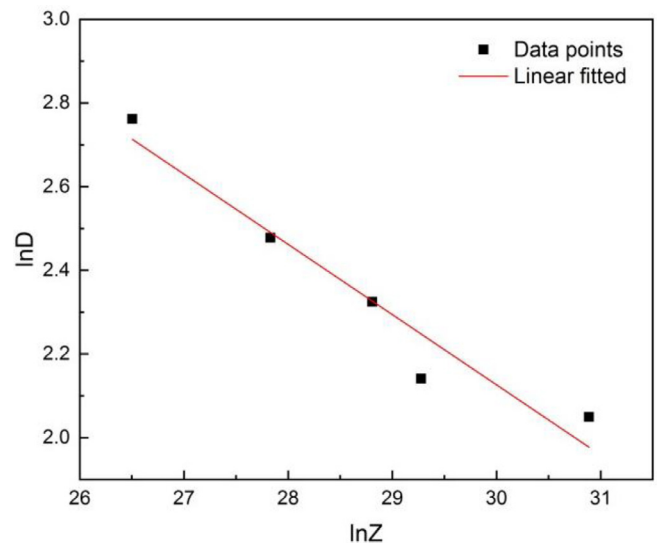

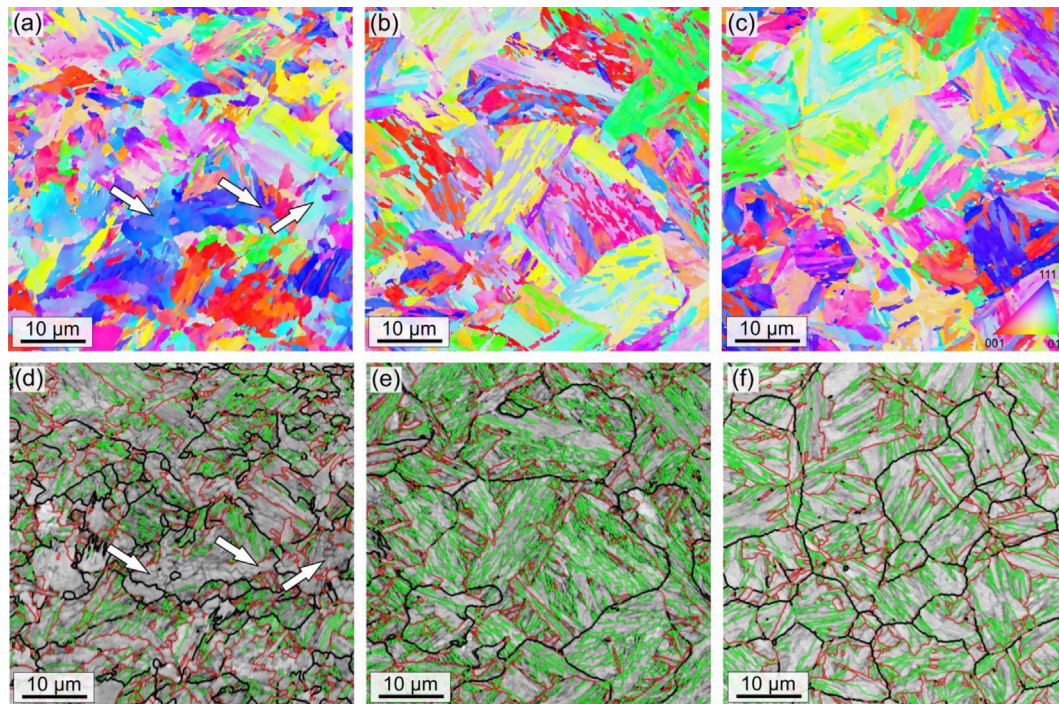**Fig. 14.** The relationship between D$_{DRXed}$ and Z parameter.

Fig. 15. (a–c) EBSD orientation mappings (IPF color coding with respect to the sample surface) and (d–f) EBSD band contrast images superimposed with the reconstructed parent austenite grain boundaries (black lines), the packet boundaries (red lines) and block boundaries (green lines) of martensite. (a + d) 850 °C/ 0.01 s^{-1}, (b + e) 950 °C/0.01 s^{-1}, (c + f) 950 °C/0.8 s^{-1}. (For interpretation of the references to color in this figure legend, the reader is referred to the web version of this article.)

contrast mapping (Fig. 15(d)). Further investigations on the martensite morphology reveals that the amount of block and packet boundaries is reduced in these areas. Liu et al. [45] demonstrated that with increasing hot deformation strain the morphology of the resulting martensite was changed from a lath-type to a cell-type morphology. Furthermore, it is found that austenite which is severely work-hardening generally hinders the nucleation and subsequent growth of martensite block due to exquisite lattice, finally leading to a less amount of blocks and packets. These facts indicate, that the DRX process has just finished or is about to be finished after deformation at 850 °C with 0.01 s^{-1} and a strain of $\varepsilon = 1$, which is consistent with the established DRX kinetics of 22MnB5 in Fig. 11(a).

An increase of the deformation temperature from 850 °C to 950 °C leads to a visible change of the obtained martensite microstructure (see Fig. 15(e)). The reconstructed PAGB illustrate a clear increase of the parent austenite grain size during the hot-deformation which can also be observed from Fig. 13. The PAGB are straighter, but still not completely equiaxed because of the further growth and deformation of DRXed grain, which can also be derived from Fig. 11(a). Additionally, the larger austenite grain size results in an increased packet size [46]. Furthermore, the amount of block boundaries is significant enhanced (Fig. 15(e)) and globulitic subgrains as well as orientation gradients can hardly be observed.

As mentioned in Section "*Microstructure observation*", a finer grain size can be generated by increasing the strain rate. For a strain rate of 0.8 s^{-1} recrystallized and equiaxed parent austenite grains can be observed. The microstructure reveals a morphology that is typical for lath martensite. Most of the grains are subdivided into packets and each packet consists of approximately parallel blocks. Due to the smaller grain size of the PAG the packet size is reduced [47]. On the contrary the width of the formed martensite blocks seems to be increased, compared to that of the strain rate of 0.01 s^{-1}. This phenomenon was also reported by Shi et al. [44]. They found that the block size increases with the decrease of packet size under deformation temperature in the range of 850–950 °C. It was believed that the negative correlation

between block size and packet size might be a result of preferred growth of the block associated with the deformation strain [44].

According to investigations of Shi [37], deformations in the austenite area basically lead to grain refinement. The lower the forming temperature in the austenite, the smaller the packet size. Similarly, the smaller the former austenite grains, the smaller the packet size is. In contrast, for the temperature range for the deformation between 850 °C and 1050 °C it was found that in comparison to the packet size, the block size decreases with increasing temperature. A correlation between packet size and block size cannot be established. After Shi, the influence of the size of former austenite grains, packets and blocks on the mechanical properties can be analysed qualitatively. Accordingly, the block size correlates with the hardness and correspondingly with the strength of the material based on the Hall-Petch type relationship. [48] An experimental study has shown that the hardness increases with decreasing block size. The block boundary is a large angle boundary which acts as a barrier to the dislocation movement. The packet size, however, influences the toughness of the material. The length of the propagated cracks can be adjusted by the width of the packet.

Regarding the examined experiments, it means that the specimens with the smallest forming temperature and biggest strain rate would obtain the smallest packet size, which results in increased toughness. If the hardness and strength are increased, the block size would have to be declined by a higher forming temperature and a low strain rate. The investigations in Fig. 14(d)–(f) show small parent austenite grain sizes for low forming temperatures of 850 °C as well as high strain rate of 0.8 s^{-1} and therefore also small packet size. While, at 950 °C/0.01 s^{-1} the stacks and blocks are significantly finer than that of 0.8 s^{-1}. Accordingly, the samples at 850 °C/0.01 s^{-1} should have a higher toughness than that under 950 °C/0.01 s^{-1}, but the influence of non-recrystallized areas with orientation gradients are not described. Furthermore, the sample at 950 °C/0.01 s^{-1} shows no orientation gradients and a small block width, making this sample predestined for increased hardness and strength.

Conclusion

In this study, the hot deformation behavior of 22MnB5 steel has been investigated by compression test at the deformation temperatures range from 800 °C to 950 °C and strain rates range from 0.01 s^{-1} to 0.8 s^{-1} which occur at press hardening processes. The main conclusions can be summarized as follows:

(1) The flow stress of studied 22MnB5 steel is greatly influenced by the deformation conditions and all the characteristic stress and strain values of the DRX were expressed as power laws of Z parameter. A physical constitutive model considering WH, DRV and DRX was developed with the values of AARE for 3.89% and R for 0.997. It cindicates that the established model has good predictive results for 22MnB5 steel for hot working.
(2) A JMAK type DRX kinetics and the DRXed grain size model were established. It is found that a larger deformation degree is needed for a completed DRX when the deformation temperature is decreased or the strain rate is increased.
(3) The martensite structure strongly depends on the deformation conditions and parent austenite grain size. A finer parent austenite grain leads to a smaller martensite packet size. Furthermore, the martensite block size becomes larger under a higher strain rate while the amount of martensite block increases with a higher temperature at the range of 850–950 °C.

Acknowledgements

Appendix A. Supplementary data

Supplementary data to this article can be found online at https://doi.org/10.1016/j.rinp.2019.102426.

References

[1] Mori K, Bariani PF, Behrens BA, Brosius A, Bruschi S, Maeno T, et al. Hot stamping of ultra-high strength steel parts. CIRP Ann – Manuf Technol 2017;66:755–77. https://doi.org/10.1016/j.cirp.2017.05.007.

[2] Kriechenbauer S, Mauermann R, Muller P. Deep drawing with superimposed low-frequency vibrations on servo-screw presses. Procedia Eng 2014;81:905–13. https://doi.org/10.1016/j.proeng.2014.10.116.

[3] Landgrebe D, Rautenstrauch A, Kunke A, Polster S, Kriechenbauer S, Mauermann R. The effect of cushion-ram pulsation on hot stamping. AIP Conf Proc 2016;1769. https://doi.org/10.1063/1.4963467.

[4] Kräusel V, Birnbaum P, Kunke A, Wertheim R. Metastable material conditions for forming of sheet metal parts combined with thermomechanical treatment. CIRP Ann – Manuf Technol 2016;65:301–4. https://doi.org/10.1016/j.cirp.2016.04.129.

[5] Birnbaum P, Baumann M, Kunke A, Kraeusel V, Landgrebe D. Combination of hot forming with CRP and rapid cooling to obtain enhanced formability in thermo-mechanical treatment. MRS Adv 2017;2:957–62. https://doi.org/10.1557/adv.2017.179.

[6] Morito S, Saito H, Ogawa T, Furuhara T, Maki T. Effect of PAGS on crystallography and morphology of lath martensite. ISIJ Int 2005;45:91–4. https://doi.org/10.2355/isijinternational.45.91.

[7] Åkerström P, Oldenburg M. Austenite decomposition during press hardening of a boron steel-computer simulation and test. J Mater Process Technol 2006;174:399–406. https://doi.org/10.1016/j.jmatprotec.2006.02.013.

[8] Naderi M, Durrenberger L, Molinari A, Bleck W. Constitutive relationships for 22MnB5 boron steel deformed isothermally at high temperatures. Mater Sci Eng A 2008;478:130–9. https://doi.org/10.1016/j.msea.2007.05.094.

[9] Duc-Toan N, Tien-Long B, Dong-Won J, Seung-Han Y, Young-Suk K. A modified johnson-cook model to predict stress-strain curves of boron steel sheets at elevated and cooling temperatures. High Temp Mater Process 2012;31:37–45. https://doi.org/10.1515/htmp.2011.127.

[10] Li H, He L, Zhao G, Zhang L. Constitutive relationships of hot stamping boron steel B1500HS based on the modified Arrhenius and Johnson-Cook model. Mater Sci Eng A 2013;580:330–48. https://doi.org/10.1016/j.msea.2013.05.023.

[11] Zhou J, Wang B, Huang M. Two constitutive descriptions of boron steel 22MnB5 at high temperature. Mater Des 2014;63:738–48. https://doi.org/10.1016/j.matdes.2014.07.008.

[12] Zhang Z, Meng S, Liu C, Zhao Y, He D. Modelling flow behaviour of quenched boron steel with different microconstituent volume fractions 2018; 0836. doi:10.1080/02670836.2017.1415015.

[13] Bachmann F, Hielscher R, Schaeben H. Texture analysis with MTEX – free and open source software toolbox. Solid State Phenom 2010;160:63–8. https://doi.org/10.4028/www.scientific.net/ssp.160.63.

[14] Nyyssönen T, Isakov M, Peura P, Kuokkala VT. Iterative determination of the orientation relationship between austenite and martensite from a large amount of grain pair misorientations. Metall Mater Trans A Phys Metall Mater Sci 2016;47:2587–90. https://doi.org/10.1007/s11661-016-3462-2.

[15] Rasti J, Najafizadeh A, Meratian M. Correcting the stress-strain curve in hot compression test using finite element analysis and Taguchi method. Int J ISSI 2011;8:26–33.

[16] Shen G, Vedhanayagam A, Kropp E, Altan T. A method for evaluating friction using a backward extrusion-type forging. J Mater Process Tech 1992;33:109–23. https://doi.org/10.1016/0924-0136(92)90314-I.

[17] Li YP, Onodera E, Matsumoto H, Chiba A. Correcting the stress-strain curve in hot compression process to high strain level. Metall Mater Trans A Phys Metall Mater Sci 2009;40:982–90. https://doi.org/10.1007/s11661-009-9783-7.

[18] Ebrahimi R, Najafizadeh A. A new method for evaluation of friction in bulk metal forming. J Mater Process Technol 2004;152:136–43. https://doi.org/10.1016/j.jmatprotec.2004.03.029.

[19] Chen XM, Lin YC, Wen DX, Zhang JL, He M. Dynamic recrystallization behavior of a typical nickel-based superalloy during hot deformation. Mater Des 2014;57:568–77. https://doi.org/10.1016/j.matdes.2013.12.072.

[20] Poliak EI, Jonas JJ. A one-parameter approach to determining the critical conditions for the initiation of dynamic recrystallization. Acta Mater 1996;44:127–36. https://doi.org/10.1016/1359-6454(95)00146-7.

[21] Zhang C, Zhang L, Shen W, Liu C, Xia Y, Li R. Study on constitutive modeling and processing maps for hot deformation of medium carbon Cr-Ni-Mo alloyed steel. Mater Des 2016;90:804–14. https://doi.org/10.1016/j.matdes.2015.11.036.

[22] Dong D, Chen F, Cui Z. A physically-based constitutive model for SA508-III steel: modeling and experimental verification. Mater Sci Eng A 2015;634:103–15. https://doi.org/10.1016/j.msea.2015.03.036.

[23] Zhou P, Ma Q. Dynamic recrystallization behavior and constitutive modeling of as-cast 30Cr2Ni4MoV steel based on flow curves. Met Mater Int 2017;23:359–68. https://doi.org/10.1007/s12540-017-6538-7.

[24] Zener C, Hollomon JH. Effect of strain rate upon plastic flow of steel. J Appl Phys 1944;15:22–32. https://doi.org/10.1063/1.1707363.

[25] Naghdy S, Akbarzadeh A. Characterization of dynamic recrystallization parameters for a low carbon resulfurized free – cutting steel. Mater Des 2014;53:910–4. https://doi.org/10.1016/j.matdes.2013.07.031.

[26] Liu YG, Li MQ, Luo J. The modelling of dynamic recrystallization in the isothermal compression of 300M steel. Mater Sci Eng A 2013;574:1–8. https://doi.org/10.1016/j.msea.2013.03.011.

[27] Moreira A, Junior J, Balancin O, Luiz VW. Sp SC. Prediction of steel flow stresses under hot working conditions 5. Plastic flow stress curve modeling. Mater Trans 2005;8:309–15.

[28] Bergström Y, Aronsson B. The application of a dislocation model to the strain and temperature dependence of the strain hardening exponent n in the Ludwik-Hollomon relation between stress and strain in mild steels. Metall Trans 1972;3:1951–7. https://doi.org/10.1007/BF02642584.

[29] Mecking H, Kocks UF. Kinetics of flow and strain-hardening. Acta Metall 1981;29:1865–75. https://doi.org/10.1016/0001-6160(81)90112-7.

[30] Hansen N, Kuhlmann-Wilsdorf D. Low energy dislocation structures due to unidirectional deformation at low temperatures. Mater Sci Eng 1986;81:141–61. https://doi.org/10.1016/0025-5416(86)90258-2.

[31] Lin YC, Chen MS, Zhong J. Prediction of 42CrMo steel flow stress at high temperature and strain rate. Mech Res Commun 2008;35:142–50. https://doi.org/10.1016/j.mechrescom.2007.10.002.

[32] Lin YC, Chen XM, Wen DX, Chen MS. A physically-based constitutive model for a typical nickel-based superalloy. Comput Mater Sci 2014;83:282–9. https://doi.org/10.1016/j.commatsci.2013.11.003.

[33] Souza RC, Silva ES, Jorge AM, Cabrera JM, Balancin O. Dynamic recovery and dynamic recrystallization competition on a Nb- and N-bearing austenitic stainless steel biomaterial: influence of strain rate and temperature. Mater Sci Eng A 2013;582:96–107. https://doi.org/10.1016/j.msea.2013.06.037.

[34] Il Kim S, Yoo YC. Dynamic recrystallization behavior of AISI 304 stainless steel. Mater Sci Eng A 2001;311:108–13. https://doi.org/10.1016/S0921-5093(01)00917-0.

[35] Ji G, Li F, Li Q, Li H, Li Z. Research on the dynamic recrystallization kinetics of Aermet100 steel. Mater Sci Eng A 2010;527:2350–5. https://doi.org/10.1016/j.msea.2009.12.001.

[36] Chen G, Chen L, Zhao G, Zhang C, Cui W. Microstructure analysis of an Al-Zn-Mg alloy during porthole die extrusion based on modeling of constitutive equation and dynamic recrystallization. J Alloys Compd 2017;710:80–91. https://doi.org/10.1016/j.jallcom.2017.03.240.

[37] Jonas JJ, Weiss I. Effect of precipitation on recrystallization in microalloyed steels. Met Sci 1979;13:238–45. https://doi.org/10.1179/msc.1979.13.3-4.238.

[38] Mejía I, Bedolla-Jacuinde A, Maldonado C, Cabrera JM. Determination of the critical conditions for the initiation of dynamic recrystallization in boron microalloyed steels. Mater Sci Eng A 2011;528:4133–40. https://doi.org/10.1016/j.msea.2011.01.102.

[39] Ebrahimi GR, Momeni A, Kazemi S, Alinejad H. Flow curves, dynamic recrystallization and precipitation in a medium carbon low alloy steel. Vacuum 2017;142:135–45. https://doi.org/10.1016/j.vacuum.2017.05.010.

[40] Chen L, Zhao G, Yu J. Hot deformation behavior and constitutive modeling of homogenized 6026 aluminum alloy. Mater Des 2015;74:25–35. https://doi.org/10.1016/j.matdes.2015.02.024.

[41] Huang K, Logé RE. A review of dynamic recrystallization phenomena in metallic materials. Mater Des 2016;111:548–74. https://doi.org/10.1016/j.matdes.2016.09.012.

[42] He DG, Lin YC, Chen J, Chen DD, Huang J, Tang Y, et al. Microstructural evolution and support vector regression model for an aged Ni-based superalloy during two-stage hot forming with stepped strain rates. Mater Des 2018;154:51–62. https://doi.org/10.1016/j.matdes.2018.05.022.

[43] Lin YC, Wu XY, Chen XM, Chen J, Wen DX, Zhang JL, et al. EBSD study of a hot deformed nickel-based superalloy. J Alloys Compd 2015;640:101–13. https://doi.org/10.1016/j.jallcom.2015.04.008.

[44] Shi Z, Liu K, Wang M, Shi J, Dong H, Pu J, et al. Effect of tensile deformation of austenite on the morphology and strength of lath martensite. Met Mater Int 2012;18:317–20. https://doi.org/10.1007/s12540-012-2015-5.

[45] Liu YG, Li MQ. Characteristics of martensite transformed from deformed austenite with various states of ultrahigh strength 300 M steel. Mater Charact 2018;144:490–7. https://doi.org/10.1016/j.matchar.2018.07.037.

[46] Järvinen H, Isakov M, Nyyssönen T, Järvenpää M, Peura P. The effect of initial microstructure on the final properties of press hardened 22MnB5 steels. Mater Sci Eng A 2016;676:109–20. https://doi.org/10.1016/j.msea.2016.08.096.

[47] Chakravarthi KVA, Koundinya NTBN, Narayana Murty SVS, Nageswara Rao B. Microstructure, properties and hot workability of M300 grade maraging steel. Def Technol 2018;14:51–8. https://doi.org/10.1016/j.dt.2017.09.001.

[48] Morito S, Yoshida H, Maki T, Huang X. Effect of block size on the strength of lath martensite in low carbon steels. Mater Sci Eng A 2006;438–440:237–40. https://doi.org/10.1016/j.msea.2005.12.048.